EUROPEAN ORGANIZATION FOR NUCLEAR RESEARCH

PH-EP/2005-057
25th November 2005

Measurement of the Strong Coupling α_S from Four-Jet Observables in e^+e^- Annihilation

The OPAL Collaboration

Abstract

Data from e^+e^- annihilation into hadrons at centre-of-mass energies between 91 GeV and 209 GeV collected with the OPAL detector at LEP, are used to study the four-jet rate as a function of the Durham algorithm resolution parameter $y_{\rm cut}$. The four-jet rate is compared to next-to-leading order calculations that include the resummation of large logarithms. The strong coupling measured from the four-jet rate is

$$\alpha_S(M_{Z^0}) = 0.1182 \pm 0.0003(\text{stat.}) \pm 0.0015(\text{exp.}) \pm 0.0011(\text{had.}) \pm 0.0012(\text{scale}) \pm 0.0013(\text{mass}),$$

in agreement with the world average. Next-to-leading order fits to the D-parameter and thrust minor event-shape observables are also performed for the first time. We find consistent results, but with significantly larger theoretical uncertainties.

The OPAL Collaboration

G. Abbiendi[2], C. Ainsley[5], P.F. Åkesson[3,y], G. Alexander[22], G. Anagnostou[1], K.J. Anderson[9], S. Asai[23], D. Axen[27], I. Bailey[26], E. Barberio[8,p], T. Barillari[32], R.J. Barlow[16], R.J. Batley[5], P. Bechtle[25], T. Behnke[25], K.W. Bell[20], P.J. Bell[1], G. Bella[22], A. Bellerive[6], G. Benelli[4], S. Bethke[32], O. Biebel[31], O. Boeriu[10], P. Bock[11], M. Boutemeur[31], S. Braibant[2], R.M. Brown[20], H.J. Burckhart[8], S. Campana[4], P. Capiluppi[2], R.K. Carnegie[6], A.A. Carter[13], J.R. Carter[5], C.Y. Chang[17], D.G. Charlton[1], C. Ciocca[2], A. Csilling[29], M. Cuffiani[2], S. Dado[21], A. De Roeck[8], E.A. De Wolf[8,s], K. Desch[25], B. Dienes[30], J. Dubbert[31], E. Duchovni[24], G. Duckeck[31], I.P. Duerdoth[16], E. Etzion[22], F. Fabbri[2], P. Ferrari[8], F. Fiedler[31], I. Fleck[10], M. Ford[16], A. Frey[8], P. Gagnon[12], J.W. Gary[4], C. Geich-Gimbel[3], G. Giacomelli[2], P. Giacomelli[2], M. Giunta[4], J. Goldberg[21], E. Gross[24], J. Grunhaus[22], M. Gruwé[8], P.O. Günther[3], A. Gupta[9], C. Hajdu[29], M. Hamann[25], G.G. Hanson[4], A. Harel[21], M. Hauschild[8], C.M. Hawkes[1], R. Hawkings[8], R.J. Hemingway[6], G. Herten[10], R.D. Heuer[25], J.C. Hill[5], D. Horváth[29,c], P. Igo-Kemenes[11], K. Ishii[23], H. Jeremie[18], P. Jovanovic[1], T.R. Junk[6,i], J. Kanzaki[23,u], D. Karlen[26], K. Kawagoe[23], T. Kawamoto[23], R.K. Keeler[26], R.G. Kellogg[17], B.W. Kennedy[20], S. Kluth[32], T. Kobayashi[23], M. Kobel[3], S. Komamiya[23], T. Krämer[25], A. Krasznahorkay[30,e], P. Krieger[6,l], J. von Krogh[11], T. Kuhl[25], M. Kupper[24], G.D. Lafferty[16], H. Landsman[21], D. Lanske[14], D. Lellouch[24], J. Letts[o], L. Levinson[24], J. Lillich[10], S.L. Lloyd[13], F.K. Loebinger[16], J. Lu[27,w], A. Ludwig[3], J. Ludwig[10], W. Mader[3,b], S. Marcellini[2], A.J. Martin[13], T. Mashimo[23], P. Mättig[m], J. McKenna[27], R.A. McPherson[26], F. Meijers[8], W. Menges[25], F.S. Merritt[9], H. Mes[6,a], N. Meyer[25], A. Michelini[2], S. Mihara[23], G. Mikenberg[24], D.J. Miller[15], W. Mohr[10], T. Mori[23], A. Mutter[10], K. Nagai[13], I. Nakamura[23,v], H. Nanjo[23], H.A. Neal[33], R. Nisius[32], S.W. O'Neale[1,*], A. Oh[8], M.J. Oreglia[9], S. Orito[23,*], C. Pahl[32], G. Pásztor[4,g], J.R. Pater[16], J.E. Pilcher[9], J. Pinfold[28], D.E. Plane[8], O. Pooth[14], M. Przybycień[8,n], A. Quadt[3], K. Rabbertz[8,r], C. Rembser[8], P. Renkel[24], J.M. Roney[26], A.M. Rossi[2], Y. Rozen[21], K. Runge[10], K. Sachs[6], T. Saeki[23], E.K.G. Sarkisyan[8,j], A.D. Schaile[31], O. Schaile[31], P. Scharff-Hansen[8], J. Schieck[32], T. Schörner-Sadenius[8,z], M. Schröder[8], M. Schumacher[3], R. Seuster[14,f], T.G. Shears[8,h], B.C. Shen[4], P. Sherwood[15], A. Skuja[17], A.M. Smith[8], R. Sobie[26], S. Söldner-Rembold[16], F. Spano[9,y], A. Stahl[3,x], D. Strom[19], R. Ströhmer[31], S. Tarem[21], M. Tasevsky[8,d], R. Teuscher[9], M.A. Thomson[5], E. Torrence[19], D. Toya[23], P. Tran[4], I. Trigger[8], Z. Trócsányi[30,e], E. Tsur[22], M.F. Turner-Watson[1], I. Ueda[23], B. Ujvári[30,e], C.F. Vollmer[31], P. Vannerem[10], R. Vértesi[30,e], M. Verzocchi[17], H. Voss[8,q], J. Vossebeld[8,h], C.P. Ward[5], D.R. Ward[5], P.M. Watkins[1], A.T. Watson[1], N.K. Watson[1], P.S. Wells[8], T. Wengler[8], N. Wermes[3], G.W. Wilson[16,k], J.A. Wilson[1], G. Wolf[24], T.R. Wyatt[16], S. Yamashita[23], D. Zer-Zion[4], L. Zivkovic[24]

[1]School of Physics and Astronomy, University of Birmingham, Birmingham B15 2TT, UK
[2]Dipartimento di Fisica dell' Università di Bologna and INFN, I-40126 Bologna, Italy
[3]Physikalisches Institut, Universität Bonn, D-53115 Bonn, Germany

[4]Department of Physics, University of California, Riverside CA 92521, USA
[5]Cavendish Laboratory, Cambridge CB3 0HE, UK
[6]Ottawa-Carleton Institute for Physics, Department of Physics, Carleton University, Ottawa, Ontario K1S 5B6, Canada
[8]CERN, European Organisation for Nuclear Research, CH-1211 Geneva 23, Switzerland
[9]Enrico Fermi Institute and Department of Physics, University of Chicago, Chicago IL 60637, USA
[10]Fakultät für Physik, Albert-Ludwigs-Universität Freiburg, D-79104 Freiburg, Germany
[11]Physikalisches Institut, Universität Heidelberg, D-69120 Heidelberg, Germany
[12]Indiana University, Department of Physics, Bloomington IN 47405, USA
[13]Queen Mary and Westfield College, University of London, London E1 4NS, UK
[14]Technische Hochschule Aachen, III Physikalisches Institut, Sommerfeldstrasse 26-28, D-52056 Aachen, Germany
[15]University College London, London WC1E 6BT, UK
[16]Department of Physics, Schuster Laboratory, The University, Manchester M13 9PL, UK
[17]Department of Physics, University of Maryland, College Park, MD 20742, USA
[18]Laboratoire de Physique Nucléaire, Université de Montréal, Montréal, Québec H3C 3J7, Canada
[19]University of Oregon, Department of Physics, Eugene OR 97403, USA
[20]CCLRC Rutherford Appleton Laboratory, Chilton, Didcot, Oxfordshire OX11 0QX, UK
[21]Department of Physics, Technion-Israel Institute of Technology, Haifa 32000, Israel
[22]Department of Physics and Astronomy, Tel Aviv University, Tel Aviv 69978, Israel
[23]International Centre for Elementary Particle Physics and Department of Physics, University of Tokyo, Tokyo 113-0033, and Kobe University, Kobe 657-8501, Japan
[24]Particle Physics Department, Weizmann Institute of Science, Rehovot 76100, Israel
[25]Universität Hamburg/DESY, Institut für Experimentalphysik, Notkestrasse 85, D-22607 Hamburg, Germany
[26]University of Victoria, Department of Physics, P O Box 3055, Victoria BC V8W 3P6, Canada
[27]University of British Columbia, Department of Physics, Vancouver BC V6T 1Z1, Canada
[28]University of Alberta, Department of Physics, Edmonton AB T6G 2J1, Canada
[29]Research Institute for Particle and Nuclear Physics, H-1525 Budapest, P O Box 49, Hungary
[30]Institute of Nuclear Research, H-4001 Debrecen, P O Box 51, Hungary
[31]Ludwig-Maximilians-Universität München, Sektion Physik, Am Coulombwall 1, D-85748 Garching, Germany
[32]Max-Planck-Institute für Physik, Föhringer Ring 6, D-80805 München, Germany
[33]Yale University, Department of Physics, New Haven, CT 06520, USA

[a] and at TRIUMF, Vancouver, Canada V6T 2A3
[b] now at University of Iowa, Dept of Physics and Astronomy, Iowa, U.S.A.
[c] and Institute of Nuclear Research, Debrecen, Hungary
[d] now at Institute of Physics, Academy of Sciences of the Czech Republic, 18221 Prague, Czech Republic

[e] and Department of Experimental Physics, University of Debrecen, Hungary
[f] and MPI München
[g] and Research Institute for Particle and Nuclear Physics, Budapest, Hungary
[h] now at University of Liverpool, Dept of Physics, Liverpool L69 3BX, U.K.
[i] now at Dept. Physics, University of Illinois at Urbana-Champaign, U.S.A.
[j] and Manchester University Manchester, M13 9PL, United Kingdom
[k] now at University of Kansas, Dept of Physics and Astronomy, Lawrence, KS 66045, U.S.A.
[l] now at University of Toronto, Dept of Physics, Toronto, Canada
[m] current address Bergische Universität, Wuppertal, Germany
[n] now at University of Mining and Metallurgy, Cracow, Poland
[o] now at University of California, San Diego, U.S.A.
[p] now at The University of Melbourne, Victoria, Australia
[q] now at IPHE Université de Lausanne, CH-1015 Lausanne, Switzerland
[r] now at IEKP Universität Karlsruhe, Germany
[s] now at University of Antwerpen, Physics Department,B-2610 Antwerpen, Belgium; supported by Interuniversity Attraction Poles Programme – Belgian Science Policy
[u] and High Energy Accelerator Research Organisation (KEK), Tsukuba, Ibaraki, Japan
[v] now at University of Pennsylvania, Philadelphia, Pennsylvania, USA
[w] now at TRIUMF, Vancouver, Canada
[x] now at DESY Zeuthen
[y] now at CERN
[z] now at DESY
[*] Deceased

1 Introduction

The annihilation of electrons and positrons into hadrons allows a precise test of Quantum Chromodynamics (QCD). Many observables have been devised which provide a convenient way of characterizing the main features of such events. Multi-jet rates are predicted in perturbation theory as functions of the jet-resolution parameter, with one free parameter, the strong coupling α_S. Events with four quarks in the final state, $q\bar{q}q\bar{q}$, or two quarks and two gluons, $q\bar{q}gg$, may lead to events with four-jet structure. In leading order perturbation theory, the rate of four-jet events in e^+e^- annihilation is predicted to be proportional to α_S^2. Thus, the strong coupling is measured by determining the four-jet production rate in hadronic events and fitting the theoretical prediction to the data.

Calculations beyond leading order are made possible by theoretical progress achieved during the last few years. For multi-jet rates as well as numerous event-shape distributions with perturbative expansions starting at $\mathcal{O}(\alpha_S)$, matched next-to-leading order (NLO) and next-to-leading logarithmic approximations (NLLA) satisfactorily describe data over large kinematically allowed regions at many centre-of-mass energies [1–4].

Measuring the four-jet rate is not the only way to determine the strong coupling; various event-shape observables sensitive to the presence of four partons in the final state may also be studied. In addition to measuring the four-jet rates, we also studied two

event-shape observables which are sensitive to the four jet structure of the final state, the D-parameter [5] and the thrust minor ($T_{\rm min}$) [6]. For these observables the NLLA predictions are only available in the nearly planar limit. Furthermore, the NLO corrections are rather large, which indicates that the neglected higher order terms in the perturbative prediction are important [7,8] and lead to a large uncertainty in the determination of the strong coupling.

In this analysis we use data collected by OPAL at LEP at 13 centre-of-mass energies covering the full LEP energy range of 91−209 GeV. A previous publication by the OPAL Collaboration performed a simultaneous measurement of $\alpha_{\rm S}$ and the QCD colour factors with data taken at 91 GeV [9]. The same theoretical predictions for the four-jet rate are used for this analysis, with the colour factors $C_{\rm A}$ and $C_{\rm F}$ set to the values expected from the QCD SU(3) symmetry group, $C_{\rm A} = 3$ and $C_{\rm F} = 4/3$. More importantly, our analysis extends the energy range up to 209 GeV and we also investigate the D-parameter and $T_{\rm min}$ event-shape observables. Similar results from other LEP collaborations can be found in [10,11].

The OPAL Collaboration has also published a comprehensive measurement of jet-rates in the energy range between 91 and 209 GeV [12] and the distributions of the D-parameter and $T_{\rm min}$ amongst many other event shape observables [13]. The data used in the present paper are identical to those presented in [12,13]. However, the determinations of $\alpha_{\rm S}$ in [12,13] were based on the two-jet rate and event shapes sensitive to three-jet processes; in contrast the present paper focuses on different calculations for observables sensitive to four-jet production.

2 Observables

2.1 The Four-Jet Rate

Jet algorithms are applied to cluster the large number of particles of a hadronic event into a small number of jets, reflecting the parton structure of the event. For this analysis we use the Durham scheme [2]. Defining each particle initially to be a proto-jet, a resolution variable y_{ij} is calculated for each pair of proto-jets i and j:

$$y_{ij} = \frac{2\min(E_i^2, E_j^2)}{E_{\rm vis}^2}(1 - \cos\theta_{ij}), \tag{1}$$

where E_i and E_j are the energies of jets i and j, $\cos\theta_{ij}$ is the angle between them and $E_{\rm vis}$ is the sum of the energies of the visible particles in the event (or the partons in a theoretical calculation). If the smallest value of y_{ij} is less than a predefined value $y_{\rm cut}$, the pair is replaced by a new proto-jet with four-momentum $p_k^\mu = p_i^\mu + p_j^\mu$, and the clustering starts again. Clustering ends when the smallest value of y_{ij} is larger than $y_{\rm cut}$, and the remaining proto-jets are accepted and counted as final selected jets.

The NLO calculation predicts the four-jet rate R_4, which is the fraction of four-jet events, as a function of $\alpha_{\rm S}$ and $y_{\rm cut}$. The NLO prediction can be written in the following way [14]:

$$R_4(y_{\rm cut}) = \frac{\sigma_{\text{4-jet}}(y_{\rm cut})}{\sigma_{\rm tot}} = \eta^2 B_4(y_{\rm cut}) + \eta^3[C_4(y_{\rm cut}) + 3/2(\beta_0 \log x_\mu - 1)\ B_4(y_{\rm cut})] \tag{2}$$

where $\sigma_{4\text{-jet}}$ is the cross-section for the production of a hadronic event with four jets at fixed $y_{\rm cut}$, $\sigma_{\rm tot}$ the total hadronic cross-section, $\eta = \alpha_{\rm S}\, C_{\rm F}/2\pi$, $x_\mu = \mu/\sqrt{s}$ with μ being the renormalization scale, $\sqrt{s}$ the centre-of-mass energy, and $\beta_0 = (11 - 2n_f/3)$ with n_f the number of active flavours[1]. The coefficients B_4 and C_4 are obtained by integrating the massless matrix elements for e^+e^- annihilation into four- and five-parton final states, calculated by the program Debrecen 2.0 [14][2]. Eq. (2) is used to predict the four-jet rate as a function of $y_{\rm cut}$. The fixed-order perturbative prediction is not reliable for small values of $y_{\rm cut}$ due to terms of the form $\alpha_{\rm S}^n \ln^m(y_{\rm cut})$ which enhance the higher order corrections. An all-order resummation of such terms (NLLA) is possible for the Durham clustering algorithm [2]. The NLLA calculation is combined with the NLO-prediction using the so-called modified R-matching scheme [9]. In this scheme the terms proportional to η^2 and η^3 are removed from the NLLA prediction $R^{\rm NLLA}$ and the difference is then added to the NLO calculation R_4 from Eq. 2 with the result:

$$R^{\rm R-match} = R^{\rm NLLA} + [\eta^2(B_4 - B^{\rm NLLA}) + \eta^3(C_4 - C^{\rm NLLA} - 3/2(B_4 - B^{\rm NLLA}))], \qquad (3)$$

where $B^{\rm NLLA}$ and $C^{\rm NLLA}$ are the coefficients of the expansion of $R^{\rm NLLA}$, taking the same form as Eq. (2), and the x_μ term and $y_{\rm cut}$ dependence have been suppressed for clarity.

2.2 Thrust minor ($T_{\rm min}$) and D-parameter

The properties of hadronic events may also be described by event-shape observables. These are used to characterize the distribution of particles in an event as "pencil-like", planar, spherical, etc. The variable $T_{\rm min}$ and the D-parameter are sensitive to hadronic configurations with more than three partons in the final state. These observables are defined as follows:

Thrust minor $T_{\rm min}$: The thrust is defined by the expression [6]

$$T = \max_{\vec{n}} \left(\frac{\sum_i |\vec{p_i} \cdot \vec{n}|}{\sum_i |\vec{p_i}|} \right) , \qquad (4)$$

where $\vec{p_i}$ is the three-momentum of particle i and the summation runs over all particles. The thrust axis $\vec{n}_T$ is the direction $\vec{n}$ which maximizes the expression in parentheses. In a further step the maximization in Eq. (4) is performed with all momenta projected onto the plane perpendicular to $\vec{n}_T$. The resulting vector is called $\vec{n}_{T_{\rm major}}$. At the last step the expression in parentheses in Eq. (4) is evaluated again for the vector $\vec{n}_{T_{\rm min}}$ which is perpendicular to both $\vec{n}_T$ and $\vec{n}_{T_{\rm major}}$, this is $T_{\rm min}$.

***D*-parameter:** This observable is based on the linearized momentum tensor

$$\Theta^{\alpha\beta} = \frac{\sum_i (p_i^\alpha p_i^\beta)/|p_i|}{\sum_i |p_i|} \quad , \quad \alpha, \beta = 1, 2, 3 \, , \qquad (5)$$

[1] In this analysis the number of active flavours is set to five.

[2] The Durham $y_{\rm cut}$ values are chosen to vary in the range between 0.00001 and 0.3162, similar to the study in Ref. [14].

where the sum runs over particles, i, and α and β denote the Cartesian coordinates of the momentum vectors. The three eigenvalues λ_j of this tensor define D through

$$D = 27\lambda_1\lambda_2\lambda_3 \; . \tag{6}$$

The NLO calculation predicts the event-shape observable distributions

$$\frac{1}{\sigma_{\rm tot}}\frac{d\sigma}{dO_4} = \eta^2 B_{O_4}(O_4) + \eta^3[C_{O_4}(O_4) + 3/2(\beta_0 \log x_\mu - 1)\; B_{O_4}(O_4)] \tag{7}$$

with O_4 being the D-parameter or $T_{\rm min}$. The coefficients B_{O_4} and C_{O_4} are obtained by integrating the massless matrix elements for e^+e^- annihilation into four-parton final states, calculated by the program Debrecen 2.0.

3 Analysis Procedure

Although the data used in the present paper are identical to those presented in [12,13], for the sake of completeness, and in order to present a coherent discussion of the systematic uncertainties, we give a brief account of the analysis procedure below.

3.1 The OPAL Detector

A detailed description of the OPAL detector can be found in Ref. [15]. This analysis relies on the reconstruction of charged particle trajectories and on the measurement of energy depositions in the electromagnetic calorimeters. Tracking of charged particles was performed with the central detector, which was located in a solenoidal magnet providing an axial magnetic field of 0.435 T. The central detector contained a silicon microvertex detector, and three drift chamber devices: an inner vertex chamber, a large volume jet chamber and surrounding z-chambers to measure the z-coordinate[3]. Most of the tracking information was obtained from the jet chamber, which provided up to 159 measured space points per track, and almost 100 % tracking efficiency in the region $|\cos\theta| < 0.98$. Electromagnetic energy was measured by lead glass calorimeters surrounding the magnet coil, separated into a barrel ($|\cos\theta| < 0.82$) and two end-cap ($0.81 < |\cos\theta| < 0.98$) sections. The electromagnetic calorimeter consisted of 11 704 lead glass blocks with a depth of 24.6 radiation lengths in the barrel and more than 22 radiation lengths in the end-caps.

3.2 Data Samples

The data used in this analysis were collected by the OPAL detector between 1995 and 2000 and correspond to 14.5 pb^{-1} of 91 GeV data, 10.4 pb^{-1} of LEP1.5 data with centre-of-mass energies of 130 GeV and 136 GeV and 706.4 pb^{-1} of LEP2 data with centre-of-mass

[3]In the OPAL right-handed coordinate system the x-axis pointed towards the centre of the LEP ring, the y-axis pointed approximately upwards and the z-axis pointed in the direction of the electron beam. The polar angle θ and the azimuthal angle ϕ are defined with respect to z and x, respectively, while r is the distance from the z-axis.

energies ranging from 161 to 209 GeV. The highest energy runs at average centre-of-mass energies between 192 and 207 GeV have an energy spread of about 1-2 GeV and we grouped these into six main energy points. The data at 91 GeV were taken during calibration runs at the Z^0 peak at the beginning of each year and during data-taking in 1996-2000. The breakdown of the data samples, the mean centre-of-mass energies, the energy range, the data-taking years and the collected luminosities are given in Table 1. For

average energy in GeV	energy range in GeV	year	luminosity (pb^{-1})	events selected	events predicted
91.3	91.0–91.5	1996-2000	14.7	395695	–
130.1	129.9–130.2	1995, 1997	5.31	318	368.4
136.1	136.0–136.3	1995, 1997	5.95	312	329.7
161.3	161.2–161.6	1996	10.1	281	275.3
172.1	170.2–172.5	1996	10.4	218	232.2
182.7	180.8–184.2	1997	57.7	1077	1083.5
188.6	188.3–189.1	1998	185.2	3086	3130.1
191.6	191.4–192.1	1999	29.5	514	473.0
195.5	195.4–196.1	1999	76.7	1137	1161.3
199.5	199.1–200.2	1999, 2000	79.3	1090	1130.8
201.6	201.3–202.1	1999, 2000	37.8	519	526.5
204.9	202.5–205.5	2000	82.0	1130	1089.6
206.6	205.5–208.9	2000	138.8	1717	1804.1

Table 1: The average center-of-mass energy, the energy range, the year of data taking and the integrated luminosity for each data sample, together with the numbers of selected data and number of events expected from Monte Carlo simulation. The horizontal lines separate the four energy intervals.

presentation purposes we combine the data above 91 GeV into three energy points [13]. In the combination the individual data sets are weighted by the product of their luminosity and signal cross-section. The LEP1.5 data samples provide an energy point at 133.3 GeV, while the LEP2 samples give energy points at 177.4 GeV and 197.0 GeV corresponding to the energy ranges from 161 to 184 GeV and from 188 to 209 GeV.

3.3 Monte Carlo Samples

The same samples of Monte Carlo simulated events as in the analysis of [13] are used to correct the data for experimental effects such as acceptance, resolution and backgrounds. The process $e^+e^- \to q\bar{q}$ is simulated using JETSET 7.4 [16] at $\sqrt{s}$=91.2 GeV, and using KK2f [17] with fragmentation performed by PYTHIA 6.125 [18] at higher energies. Corresponding samples using HERWIG 6.2 [19] are used for systematic checks. Electroweak four-fermion background processes are simulated using KORALW 1.42 [20] with GRC4f [21] matrix elements and fragmentation performed by PYTHIA. The Monte Carlo samples generated at each energy point are processed through a full simulation of the OPAL detector [22] and reconstructed in the same way as the data. In addition, for

comparisons with the corrected data and to estimate fragmentation effects, large samples of generator-level Monte Carlo events are employed, using the parton shower models PYTHIA 6.158, HERWIG 6.2 and ARIADNE 4.11 [23]. Each of these fragmentation models contains a number of tunable parameters; these were adjusted by tuning to previously published OPAL data at $\sqrt{s} \sim 91$ GeV as described in Ref. [24] for PYTHIA/JETSET and in Ref. [25] for HERWIG and ARIADNE.

3.4 Selection of Events

The selection of events for this analysis follows exactly the study described in [13]. It consists of three main stages: the identification of hadronic event candidates, the removal of events with a large amount of initial state radiation (ISR), and the removal of four-fermion background events.

The selection of hadronic events is based on cuts on particle multiplicity mainly to remove leptonic final states and visible energy and longitudinal momentum balance mainly to remove two-photon events, $\mathrm{e^+e^-} \to \mathrm{e^+e^-}\gamma^*\gamma^*$, with hadronic final states.

Standard criteria [13] are used to select well measured tracks and clusters of energy deposits in the calorimeter. The number of good charged particle tracks is required to be greater than six. The polar angle of the thrust axis is required to satisfy $|\cos(\theta_{\mathrm{T}})| < 0.9$ in order that the events be well contained within the detector acceptance.

The effective $\mathrm{e^+e^-}$ centre-of-mass energy after excluding all ISR photons, $\sqrt{s'}$, is estimated for each selected event using the algorithm described in Ref. [26]. At centre-of-mass energies of 130 GeV and above, we require that $\sqrt{s} - \sqrt{s'} < 10$ GeV in order to select non-radiative events.

At energies above the $\mathrm{W^+W^-}$ production threshold, electroweak four-fermion events, especially those involving $\mathrm{q\bar{q}q\bar{q}}$ final states, become a substantial background. These are reduced by using the standard OPAL $\mathrm{W^+W^-}$ likelihood-based selections [27]. At centre-of-mass energies of 161 GeV and above, the $\mathrm{W^+W^-} \to \mathrm{q\bar{q}q\bar{q}}$ likelihood is required to satisfy $\mathcal{L}_{\mathrm{q\bar{q}q\bar{q}}} < 0.25$ and the $\mathrm{W^+W^-} \to \mathrm{q\bar{q}}\ell\nu$ likelihood is required to satisfy $\mathcal{L}_{\mathrm{q\bar{q}}\ell\nu} < 0.5$.

The numbers of selected candidate events obtained after applying the selection cuts are given in Table 1. The numbers are consistent with expectations based on Monte Carlo simulation[4]. After all cuts, the acceptance for non-radiative signal events[5] ranges from 88.5% at 91 GeV, where the loss in acceptance is mostly due to the cut on the polar angle of the thrust axis, to 76.5% at 207 GeV, where additional cuts on $\sqrt{s'}$ and four-fermion background rejection reduce the efficiency. The residual four-fermion background is negligible below 161 GeV, and increases from 2.1% at 161 GeV to 6.2% at 207 GeV.

[4]The numbers of events expected on the basis of Monte Carlo simulations are given in all cases except for 91 GeV; to perform an accurate prediction close to the $\mathrm{Z^0}$ peak would require a much more careful investigation of the beam energy and luminosity than is required for the present analysis.

[5]Defined for this purpose as those fulfilling $\sqrt{s} - \sqrt{s'} < 1$ GeV, with $\sqrt{s'}$ the effective $\mathrm{e^+e^-}$ centre-of-mass energy after excluding all ISR photons.

3.5 Corrections to the data

In order to mitigate the effects of double counting of energy in tracks and calorimetry, a standard algorithm is adopted [13] which associates charged particles with electromagnetic calorimeter clusters, and subtracts the estimated contribution of the charged particles from the calorimetry energy. All selected tracks, and the electromagnetic calorimeter clusters remaining after this procedure, are used in the evaluation of the distributions. The resulting distributions with all selection cuts applied are called detector-level distributions.

The expected number of remaining four-fermion background events, ζ_i, is subtracted from the number of data events, N_i, for each data point of each distribution[6]. The effects of detector acceptance and resolution and of residual ISR are then accounted for at each data point. Since in the present analysis the Monte Carlo model gives a good description of the data, and migration between data points is small, this procedure is justified.

Two distributions are formed from Monte Carlo simulated signal events for each observable; the first, at the detector level, treats the Monte Carlo events identically to the data, while the second, at the hadron level, is computed using the true four-momenta of the stable particles[7] in the event, and is restricted to events whose s' satisfied $\sqrt{s} - \sqrt{s'} < 1$ GeV. The Monte Carlo ratio of the hadron level to the detector level for each data point, α_i, is used as a correction factor for the data, yielding the corrected data point $\tilde{N}_i = \alpha_i(N_i - \zeta_i)$.

The hadron-level distribution is then normalized to unity: $P_i = \tilde{N}_i/N$, where the sum $N = \sum_k \tilde{N}_k$ includes the underflow and overflow data points where appropriate.

3.6 Fit Procedure

Our measurement of the strong coupling α_S is based on fits of QCD predictions to the corrected distributions. The theoretical predictions as described in Section 2 provide distributions at the parton level. The parton-level distributions are obtained from the partons after the parton shower, just before the hadronization. In order to confront the theory with the hadron-level data, it is necessary to correct for hadronization effects. This is done by calculating the distributions at both the hadron and the parton level using PYTHIA and, as a cross-check, with the HERWIG and ARIADNE models. The theoretical prediction is then multiplied by the ratio of the hadron- and parton-level distributions.

A χ^2-value for each energy point is calculated using the following formula

$$\chi^2 = \sum_{i,j}^{n} (O_{4,i} - O_4(\alpha_S)_i^{\text{theo}})(V_{ij}(O_4))^{-1}(O_{4,j} - O(\alpha_S)_j^{\text{theo}}), \tag{8}$$

with i, j running over all data points in the fit range and O_4 corresponding to either the four-jet rate R_4, the differential distribution $T_{\min}$ or the D-parameter, while $V_{ij}(O_4)$ is the covariance matrix. The χ^2 value is minimized with respect to α_S for each energy point separately.

[6] A data point is the center of a bin of a distribution for the D-parameter and $T_{\min}$, while for the four-jet rate we have points at discrete values of y_{cut} where the analysis is performed.

[7] All charged and neutral particles with a lifetime longer than 3×10^{-10} s are treated as stable.

The four-jet rate is an integrated distribution, while the D-parameter and $T_{\min}$ distributions are differential ones. Therefore in the four-jet rate distribution a single event can contribute to several $y_{\rm cut}$-data point and for this reason the data points are correlated. The complete covariance matrix W_{ij} is determined from four-jet rate distributions calculated at the hadron level. Subsamples are built by choosing 1000 events randomly out of the set of all generated Monte Carlo events. A single event may be included in several subsamples, but the impact on the final covariance matrix is expected to be small and, therefore, is neglected [28]. For every energy point 1000 subsamples are built. The covariance matrix is then used to determine the correlation matrix, $\rho_{ij} = W_{ij}/\tilde{\sigma}_i\tilde{\sigma}_j$, with $\tilde{\sigma}_i = \sqrt{W_{ii}}$. The covariance matrix $V_{ij}(R_4)$ used in the χ^2 fit is then determined using the statistical error σ_i of the data sample at data point i and the correlation matrix $\rho_{ij} : V_{ij}(R_4) = \rho_{ij}\sigma_i\sigma_j$.

For the fit to the event-shape observables the covariance matrix $V_{ij}(O_4)$ for P_i is computed by transforming the diagonal Poisson covariance matrix for the uncorrected data points N_i [13]:

$$V_{ij} = \sum_k \frac{\partial P_i}{\partial N_k}\frac{\partial P_j}{\partial N_k}N_k = \frac{1}{N^4}\sum_k \alpha_k^2 N_k \left(N\delta_{ik} - \widetilde{N}_i\right)\left(N\delta_{jk} - \widetilde{N}_j\right) \ . \tag{9}$$

3.7 Combination of Energy Points

For presentation purposes the data of several energy points are combined. The four-jet rate and event shape distributions measured at the different energy points are averaged using the products of luminosity and cross-section. The fit results for $\alpha_{\rm S}$, however, are combined using the procedure of Ref. [13].

In brief the method is as follows. The $\alpha_{\rm S}$ measurements to be combined are first evolved to the common scale of the combination, $Q_0 = \sqrt{s_0}$, assuming the validity of QCD. The measurements are then combined using a weighted mean method, based on minimizing the χ^2 between the combined values and the measurements. If the measured values evolved to a common scale $Q_0 = \sqrt{s_0}$ are denoted y_i, with covariance matrix V', the combined values, $\alpha_{\rm S}(\sqrt{s_0})$, are given by

$$\alpha_{\rm S}(\sqrt{s_0}) = \sum_i w_i y_i \quad \text{where} \quad w_i = \frac{\sum_j (V'^{-1})_{ij}}{\sum_{j,k}(V'^{-1})_{jk}}, \tag{10}$$

and i, j enumerate the individual measurements. Only experimental systematic errors (assumed to be fully correlated, $V'_{ij} = \sigma'_i\sigma'_j$, between measurements) are taken to contribute to the off-diagonal elements in V'. All error contributions (statistical, experimental, hadronization, scale uncertainty and the uncertainty from massless calculations) are taken to contribute to the diagonal elements. The hadronization and scale uncertainties are computed from the $\alpha_{\rm S}$ values obtained with the alternative hadronization models and with the upper and lower values of the renormalization scale, respectively, and combined according to Eq. 10. The uncertainty for the massless calculations is also combined according to Eq. 10.

4 Systematic Uncertainties

Several sources of possible systematic uncertainty are studied as in [13]. All systematic uncertainties are taken as symmetric.

Experimental uncertainties: Contributions to the experimental uncertainties are estimated by repeating the analysis with varied cuts or procedures. For each systematic variation the value of α_S is determined and then compared to the result of the standard analysis (default value). In each case, the difference with respect to the default value is taken as a systematic uncertainty.

(1) The algorithm to avoid the double counting of energy in tracks and calorimetry is not applied. Instead all observables are computed using all charged tracks and electromagnetic calorimeter clusters. The effects of double counting are then taken into account exclusively through the detector correction.

(2) The containment cut is tightened to be well within the barrel, $|\cos(\theta_T)| < 0.7$.

(3) Instead of using PYTHIA for the correction of detector effects as described in Section 3.5, events generated with HERWIG are used.

(4) The fit range[8] is changed. Two different cases are considered. First the fit range is decreased by one data point at each edge of the fit range. Second the fit range is extended by one data point at each edge of the fit range. The larger deviation from the default fit is taken as a systematic uncertainty. In order to take statistical fluctuations into account, the deviation is calculated using the average deviation of a fit applied to 50 Monte Carlo samples.

(5) The algorithm to compute s' is replaced by a simpler version accounting for at most one initial-state photon [26].

(6) The cut on the likelihood variable $\mathcal{L}_{q\bar{q}q\bar{q}}$ to reject background from $W^+W^- \to q\bar{q}q\bar{q}$ events is changed from 0.25 to 0.1 and 0.4. The larger deviation from the default value is taken as the systematic uncertainty.

(7) The cut on the likelihood variable $\mathcal{L}_{q\bar{q}\ell\nu}$ to reject background from $W^+W^- \to q\bar{q}\ell\nu$ events is changed from 0.5 to 0.25 and 0.75. The larger deviation from the default value is taken as the systematic uncertainty.

(8) The amount of subtracted four-fermion background is varied by $\pm 5\%$. The larger deviation from the default value is taken as the systematic uncertainty.

Variation (5) applies only to the data taken above the Z^0 resonance and variations (6)-(8) only to data taken at and above the W-pair threshold at 161 GeV. All experimental uncertainties are added in quadrature and the result is quoted as the experimental systematic uncertainty. None of the variations contribute dominantly to the overall experimental systematic uncertainty.

[8] The determination of the fit range is explained in section 5.1.1

Hadronization: The uncertainties associated with the hadronization correction are evaluated by using HERWIG and ARIADNE instead of PYTHIA. The larger change in α_S resulting from these alternatives is taken as the error.

Scale uncertainties: The uncertainty, associated with missing higher order terms in the theoretical prediction, is assessed by varying the renormalization scale factor x_μ. The predictions of a complete QCD calculation would be independent of x_μ, but a finite-order calculation such as that used here retains some dependence on x_μ. The renormalization scale x_μ is set to half and twice the value of x_μ from the default fit. The larger deviation from the default value of α_S is taken as the systematic uncertainty. The uncertainty band method as discussed in [29] cannot be applied to this analysis, because the rescaling of the NLLA terms and the use of different matching schemes are currently not possible. However, the renormalization scale variation in the range $0.5 < x_\mu < 2.0$ gives scale uncertainties for most observables consistent with uncertainties obtained with the uncertainty band method [29].

Uncertainties from massless QCD calculations: In the case of the four-jet rate an additional uncertainty from massless QCD calculations is considered. The QCD prediction used is only available for the massless case. Effects from massive b quarks are expected and the corresponding uncertainties on the strong coupling are evaluated for the four-jet rate. The overall four-jet rate can be written as the sum of the the four-jet rate originating from b quark and from light quark events, $R_4 = f_b R_4^b + (1 - f_b) R_4^{light} = (f_b B_4 + (1 - f_b)) R_4^{light}$, with f_b being the fraction of b quark events, R_4^b the four-jet rate originating from b quark events, R_4^{light} the four-jet rate originating from light quark events and $B_4 = R_4^b / R_4^{light}$. The Standard Model expectation for the fraction f_b computed in [30] varies between 0.216 for data taken at LEP1 and 0.169 at 207 GeV. Following the studies of QCD heavy mass effects [31] $B_4 \approx 0.9$ at $\sqrt{s} = M_{Z^0}$, leading to a change in the overall four-jet rate R_4 of $\approx 2\%$. Even though the effect is expected to decrease with increasing $\sqrt{s}$, a value of $B_4 = 0.9$ is used as a conservative estimate for the whole energy range. Since $R_4 \sim \alpha_S^2$ in LO QCD we have $\Delta\alpha_S/\alpha_S = \Delta R_4 / 2R_4$ and thus we expect a $\approx 1\%$ relative change in α_S. This is taken to be our massless QCD uncertainty.

5 Results

5.1 Four-Jet Rate Distributions

The four-jet rates for the four energy intervals, after subtraction of background and correction for detector effects, are shown in Figure 1. Superimposed we show the distribution predicted by the PYTHIA, HERWIG and ARIADNE Monte Carlo models. In order to allow for a more quantitative comparison between data and models, the inserts in the upper right corner show the differences between data and each model, divided by the combined statistical and experimental error in each data point The sum of squares of these differences would, in the absence of correlations, represent a χ^2 between data and the model. However, since correlations are present, such χ^2 values should be regarded only as a rough indication of the agreement between data and the models. The three models are seen to describe the high energy data well. Some discrepancies are, however, seen in the 91 GeV data which have a much better precision. The different Monte Carlo

models do not agree with each other; ARIADNE tends to give the best description of the data.

5.1.1 Determination of α_S

For the QCD prediction of $R_4(y_{cut})$ the combined $\mathcal{O}(\alpha_S^3)$+NLLA calculation (Eq. 3) is used. The scale parameter x_μ is set to one. The fit range is $0.0028 < y_{cut} < 0.0371$ for data taken at 91 GeV, $0.0018 < y_{cut} < 0.0178$ for data taken at LEP1.5 and $0.0018 < y_{cut} < 0.0056$ for data taken at LEP2. The fit range is determined by requiring that the hadronization corrections be less than 20% and the detector corrections be less than 50%. As shown in [14] the theoretical uncertainty due to higher order missing terms increases significantly for y_{cut} values below 0.005. Therefore we impose a further constraint on the y_{cut} region – that the theoretical prediction should not vary by more than 5% as the renormalization scale factor x_μ is varied from 0.5 to 2 [9]. The fit range for the LEP2 data contains only three data points; an enlarged fit range would lead to only a minor gain in statistical precision. We require the same fit range for all energy points above 136 GeV. In Figure 2 the hadron-level four-jet rate distributions for the four energy intervals are shown together with the fit result. The fit ranges cover the falling slope of the distributions at large y_{cut}, where the perturbative QCD predictions adequately describe the data. The increasing slope of the distributions at low y_{cut} values is less well described by the perturbative QCD description. In this region the hadronization corrections become large (more than 100%) and the various hadronization models start to differ significantly. The fits performed at individual energy points are combined in the four different energy bins: 91.2 GeV; 130 and 136 GeV; 161, 172 and 183 GeV; and 189–209 GeV using the method described in Section 3.7. The results are summarized in Table 2 and shown in Figure 3. At LEP1 the statistical uncertainty is much smaller than the theoretical one. The hadronization scales as an inverse power of $\sqrt{s}$ and therefore the hadronization uncertainty decreases with increasing energy. The fit range for data taken at LEP2 extends towards lower y_{cut} values compared to the fit range for data taken at LEP1. This leads to an increased theoretical uncertainty for α_S. Finally we combine all

average $\sqrt{s}$ in GeV	α_S	stat.	exp.	hadr.	scale	mass
91	0.1182	0.0002	0.0013	0.0012	0.0011	0.0013
133	0.1067	0.0042	0.0045	0.0010	0.0011	0.0010
177	0.1081	0.0027	0.0037	0.0007	0.0013	0.0009
197	0.1070	0.0013	0.0039	0.0006	0.0016	0.0009

Table 2: The mean value of α_S for each energy interval, the statistical and experimental errors, and the errors due to hadronization and scale uncertainties and massless QCD.

[9] The uncertainty of the hadronization models and the detector correction using different Monte Carlo models is also less than 5%.

measurements to a single value of $\alpha_S(M_{Z^0})$, with the final result:

$$\alpha_S(M_{Z^0}) = 0.1182 \pm 0.0003(\text{stat.}) \pm 0.0015(\text{exp.}) \pm 0.0011(\text{had.}) \pm 0.0012(\text{scale}) \pm 0.0013(\text{mass}), \quad (11)$$

which is clearly dominated by the α_S value obtained at 91 GeV. The weight as calculated in Eq. 10 for the data taken at 91 GeV is 84.3%.

5.1.2 Scale Dependence of α_S

For the fits in Section 5.1.1 the renormalization scale is set to the natural choice $x_\mu = 1$. However, different schemes for the determination of the renormalization scale are proposed [32]. In this section we investigate two of these.

In the optimized renormalization scheme, discussed in detail in [33], the minimization is performed with both α_S and x_μ treated as free parameters. However, at some low-statistics LEP2 energy points the fits did not converge. For this reason we applied a modified version of the optimized renormalization scheme. The optimized scale x_μ^{opt} was determined with the high statistics sample at 91 GeV and then the same scale was used at higher energies. The result for x_μ^{opt} at 91 GeV is $x_\mu^{\text{opt}} = 0.672 \pm 0.033(\text{stat.})$. The variation of χ^2/d.o.f. as a function of the scale x_μ for 91 GeV data is shown in Figure 4. The combination of all energy points using the method described in Section 3.7 returns a value of

$$\alpha_S(M_{Z^0}) = 0.1187 \pm 0.0005(\text{stat.}) \pm 0.0018(\text{exp.}) \pm 0.0011(\text{had.}) \pm 0.0012(\text{mass}). \quad (12)$$

The weight as calculated in Eq. 10 for the data taken at 91 GeV is 73.1%, leading to an increased statistical uncertainty in the combined result.

The second choice for the determination of the renormalization scale followed approximately the approach suggested by Stevenson [34]. The renormalization scale x_μ^{min} is specified by the point with α_S having the least sensitivity to the renormalization scale x_μ. Using the 91 GeV data (Figure 4) x_μ^{min} is determined to be $x_\mu^{\text{opt}} = 1.36$. The fit is repeated at all other energy points with x_μ set to x_μ^{min}. The combination of all energy points using the method described in Section 3.7 returns a value of

$$\alpha_S(M_{Z^0}) = 0.1182 \pm 0.0003(\text{stat.}) \pm 0.0014(\text{exp.}) \pm 0.0012(\text{had.}) \pm 0.0013(\text{mass}). \quad (13)$$

Both alternative choices for the renormalization scale return a value of α_S which is well within the variation of the systematic uncertainty due to missing higher order terms.

5.2 Thrust minor and *D*-parameter

For the T_{min} and D-parameter event-shape variables only the basic NLO calculations are available. For this reason and due to the problems discussed in the introduction we expect large systematic uncertainties due to missing higher order terms. The strong coupling α_S has not previously been determined using these four-jet event-shape variables. Here we perform a first measurement of α_S to quantify the various experimental, hadronization and theoretical uncertainties.

Studies with the basic NLO calculations were already performed with three-jet event-shape observables [33,35]. These investigations showed that fits with the renormalization scale fixed to $x_\mu = 1$ described the data worse than fits with both parameters α_S and x_μ free, which is usually interpreted to mean that the optimized scale-choice mimics the effect of higher order corrections. We use both approaches here. The D-parameter and $T_{\min}$ event-shape distributions were published in [13] and are used here. For the QCD predictions we use the Debrecen 2.0 $\mathcal{O}(\alpha_S^3)$ calculations [14]. In the first approach the scale parameter x_μ, as discussed in Section 2.2, is set to one. The fit range is set from 0.010 to 0.25 for the D-parameter and from 0.06 to 0.16 for $T_{\min}$. The fit range is determined by requiring that the hadronization and the detector correction be less than 50%. The results obtained at average centre-of-mass energies of 91 GeV and 197 GeV are shown in Figure 5. For the D-parameter the slope of the curve obtained from the theory prediction after the χ^2 minimization does not give a good description of the data. Similar effects were already seen previously with three- and four-jet observables [8,10,33,35]. The results for the fit to the data between 91 and 209 GeV are combined to a single value for $\alpha_S(M_{Z^0})$ using the method introduced in Section 3.7. The result for the D-parameter is

$$\alpha_S(M_{Z^0}) = 0.1047 \pm 0.0014(\text{stat.}) \pm 0.0037(\text{exp.}) \pm 0.0061(\text{had.}) \pm 0.0052(\text{scale}) \quad (14)$$

and for $T_{\min}$

$$\alpha_S(M_{Z^0}) = 0.1318 \pm 0.0016(\text{stat.}) \pm 0.0056(\text{exp.}) \pm 0.0023(\text{had.}) \pm 0.0111(\text{scale}), \quad (15)$$

both consistent with the result from the four-jet rate, albeit with large errors. All uncertainties are greater than those on the four-jet rate determination. In particular the systematic uncertainty due to higher order missing terms is significantly larger.

The impact of the scale x_μ on the result is studied with a revised fit using the modified optimized renormalization scheme as in Section 5.1.2. The optimized scale x_μ^{opt} is determined with 91 GeV data only and the fit repeated with α_S free and the scale set to x_μ^{opt}. For the D-parameter the scale is set to $x_\mu^{\text{opt}} = 0.0220 \pm 0.0002(\text{stat.})$ and for $T_{\min}$ to $x_\mu^{\text{opt}} = 0.0089 \pm 0.0001(\text{stat.})$[10]. The description of the slope of the D-parameter improves significantly when the optimized renormalization scale parameter is used. The results are combined to a single value for $\alpha_S(M_{Z^0})$ using the method introduced in Section 3.7. The result for the D-parameter is

$$\alpha_S(M_{Z^0}) = 0.0987 \pm 0.0011(\text{stat.}) \pm 0.0044(\text{exp.}) \pm 0.0022(\text{had.}) \quad (16)$$

and for $T_{\min}$

$$\alpha_S(M_{Z^0}) = 0.1100 \pm 0.0011(\text{stat.}) \pm 0.0045(\text{exp.}) \pm 0.0032(\text{had.}). \quad (17)$$

Due to the problems discussed above we do not combine the α_S values based on the event-shape distributions with the one from the four-jet rate. The differences between the result evaluated at the natural scale and at the optimized scale suggests, as discussed in [7,8], that the uncalculated higher order terms are important. An improved theoretical understanding is necessary before α_S measurements using four-jet event-shapes are competitive.

[10] Other studies with observables using NLO predictions only with an optimized scale also result in x_μ values well below unity [10,33].

6 Summary

In this paper we present the measurements by the OPAL Collaboration of the strong coupling α_S from the four-jet rate at centre-of-mass energies between 91 and 209 GeV. The predictions of the PYTHIA, HERWIG and ARIADNE Monte Carlo models are found to be in general agreement with the measured distributions.

From a fit of matched $\mathcal{O}(\alpha_S^3)$+NLLA predictions to the four-jet rate, we have determined the strong coupling $\alpha_S(M_{Z^0}) = 0.1182 \pm 0.0025$(total error), which is consistent with the world average value of $\alpha_S(M_{Z^0}) = 0.1182 \pm 0.0027$ [36], based on a detailed evaluation of systematic errors. A fit to the D-parameter and the $T_{\min}$ was performed using basic $\mathcal{O}(\alpha_S^3)$ predictions. We find consistent results with significantly larger theoretical uncertainties. Figure 6 summarizes the results obtained and compares them with results from previous OPAL publications using jet-rates [12], event shape distributions and moments [13]. The results are in good agreement with each other. Our result using the four-jet rate has the smallest uncertainty. This is mostly due to the comparatively small scale uncertainty, originating from the fact that the natural scale x_μ=1 is close to the scale with the least sensitivity to α_S, as shown in Figure 4.

Acknowledgements:

We particularly wish to thank the SL Division for the efficient operation of the LEP accelerator at all energies and for their close cooperation with our experimental group. In addition to the support staff at our own institutions we are pleased to acknowledge the
Department of Energy, USA,
National Science Foundation, USA,
Particle Physics and Astronomy Research Council, UK,
Natural Sciences and Engineering Research Council, Canada,
Israel Science Foundation, administered by the Israel Academy of Science and Humanities,
Benoziyo Center for High Energy Physics,
Japanese Ministry of Education, Culture, Sports, Science and Technology (MEXT) and a grant under the MEXT International Science Research Program,
Japanese Society for the Promotion of Science (JSPS),
German Israeli Bi-national Science Foundation (GIF),
Bundesministerium für Bildung und Forschung, Germany,
National Research Council of Canada,
Hungarian Foundation for Scientific Research, OTKA T-038240, and T-042864,
The NWO/NATO Fund for Scientific Research, the Netherlands.

References

[1] S. Catani *et al.*, *Phys. Lett.* B **263** (1991) 491.

[2] S. Catani *et al.*, *Phys. Lett.* B **269** (1991) 432.

[3] L. Dixon and A. Signer, *Phys. Rev.* D **56** (1997) 4031.

[4] Z. Nagy and Z. Trócsányi, *Nucl. Phys. B (Proc. Suppl.)* **74** (1999) 48.

[5] G. Parisi, *Phys. Lett.* **B74** (1978) 65;
J.F. Donoghue, F.E. Low and S.Y. Pi, *Phys. Rev.* **20** (1979) 2759;
R.K. Ellis, D.A. Ross and A.E. Terrano, *Nucl. Phys.* B **178** (1981) 421.

[6] S. Brandt *et al.*, *Phys. Lett.* **12** (1964) 57.
D. Fahri *et al.*, *Phys. Rev. Lett.* **39** (1977) 1587.

[7] Z. Nagy and Z. Trócsányi, *Phys. Rev. Lett.* **79** (1997) 3604.

[8] J.M. Campbell *et al.*, *Eur. Phys. J.* C **9** (1999) 245.

[9] OPAL Collaboration, G. Abbiendi *et al.*, *Eur. Phys. J.* C **20** (2001) 601.

[10] DELPHI Collaboration, J. Abdallah *et al.*, EPJC **38** (2005) 413.

[11] ALEPH Collaboration, A. Heister *et al.*, EPJC **27** (2003) 1.

[12] OPAL Collaboration, G. Abbiendi *et al.*, CERN-EP-2005-024, *submitted to to Eur. Phys. J C.*

[13] OPAL Collaboration, G. Abbiendi *et al.*, *Eur. Phys. J.* C **40** (2005) 287.

[14] Z. Nagy and Z. Trócsányi, *Phys. Rev.* D **59** (1999) 14020;
Erratum, ibid. **62** (2000) 099902.

[15] OPAL Collaboration, K. Ahmet *et al.*, *Nucl. Inst. Meth.* **305** (1991) 275,
S. Anderson *et al.*, *Nucl. Inst. Meth.* A **403** (1998) 326.

[16] T. Sjöstrand, *Comp. Phys. Comm.* **39** (1986) 347;
T. Sjöstrand and M. Bengtsson, *Comp. Phys. Comm.* **43** (1987) 367.

[17] S. Jadach *et al.*, *Phys. Lett.* B **449** (1999) 97;
S. Jadach *et al.*, *Comp. Phys. Comm.* **130** (2000) 260.

[18] T. Sjöstrand, *Comp. Phys. Comm.* **82** (1994) 74.

[19] G. Marchesini *et al.*, *Comp. Phys. Comm.* **67** (1992) 465.

[20] S. Jadach *et al.*, *Comp. Phys. Comm.* **119** (1999) 272.

[21] J. Fujimoto *et al.*, *Comp. Phys. Comm.* **100** (1997) 128.

[22] J. Allison *et al.*, *Nucl. Inst. Meth.* A **317** (1992) 47.

[23] L. Lönnblad, *Comp. Phys. Comm.* **71** (1992) 15.

[24] OPAL Collaboration, G. Alexander *et al.*, *Z. Phys.* C **69** (1996) 543.

[25] OPAL Collaboration, G. Abbiendi *et al.*, *Eur. Phys. J.* C **35** (2004) 293.

[26] OPAL Collaboration, G. Abbiendi *et al.*, *Eur. Phys. J.* C **33** (2004) 173.

[27] OPAL Collaboration, G. Abbiendi *et al.*, *Eur. Phys. J.* C **8** (1999) 191,
OPAL Collaboration, G. Abbiendi *et al.*, *Phys. Lett.* B **493** (2000) 249.

[28] K.G. Hayes, M. Perl and B. Efron, *Phys. Rev.* D **39** (1989) 274.

[29] R.W.L. Jones *et al.*, *JHEP* **12** (2003) 007.

[30] S. Schael *et al.*, *A Combination of Preliminary Electroweak Measurements and Constraints on the Standard Model*, CERN-PH-EP/2004-069.

[31] A. Ballestrero *et al.*, in: *Reports of the Working Group on Precision Calculations for LEP2 physics (CERN, Geneva, 2000)*, eds. S. Jadach *et al.*, CERN-2000-09, p.95 [hep-ph/0006259v2].

[32] J. Chyla and A.L. Kataev, in: *Reports of the Working Group on Precision Calculations for the Z Resonance (CERN, Geneva, 1994)*, eds. D.Yu. Bardin *et al.*, CERN-95-03, p.313 [hep-ph/9502383].

[33] OPAL Collaboration, P.D. Acton *et al.*, *Z. Phys.* C **55** (1992) 1.

[34] P.M. Stevenson, *Phys. Rev.* D **23** (1981) 2916.

[35] DELPHI Collaboration, P. Abreu *et al.*, *Eur. Phys. J.* C **14** (2000) 557.

[36] S. Bethke, *Nucl. Phys. Proc. Suppl.* **135** (2004) 345.

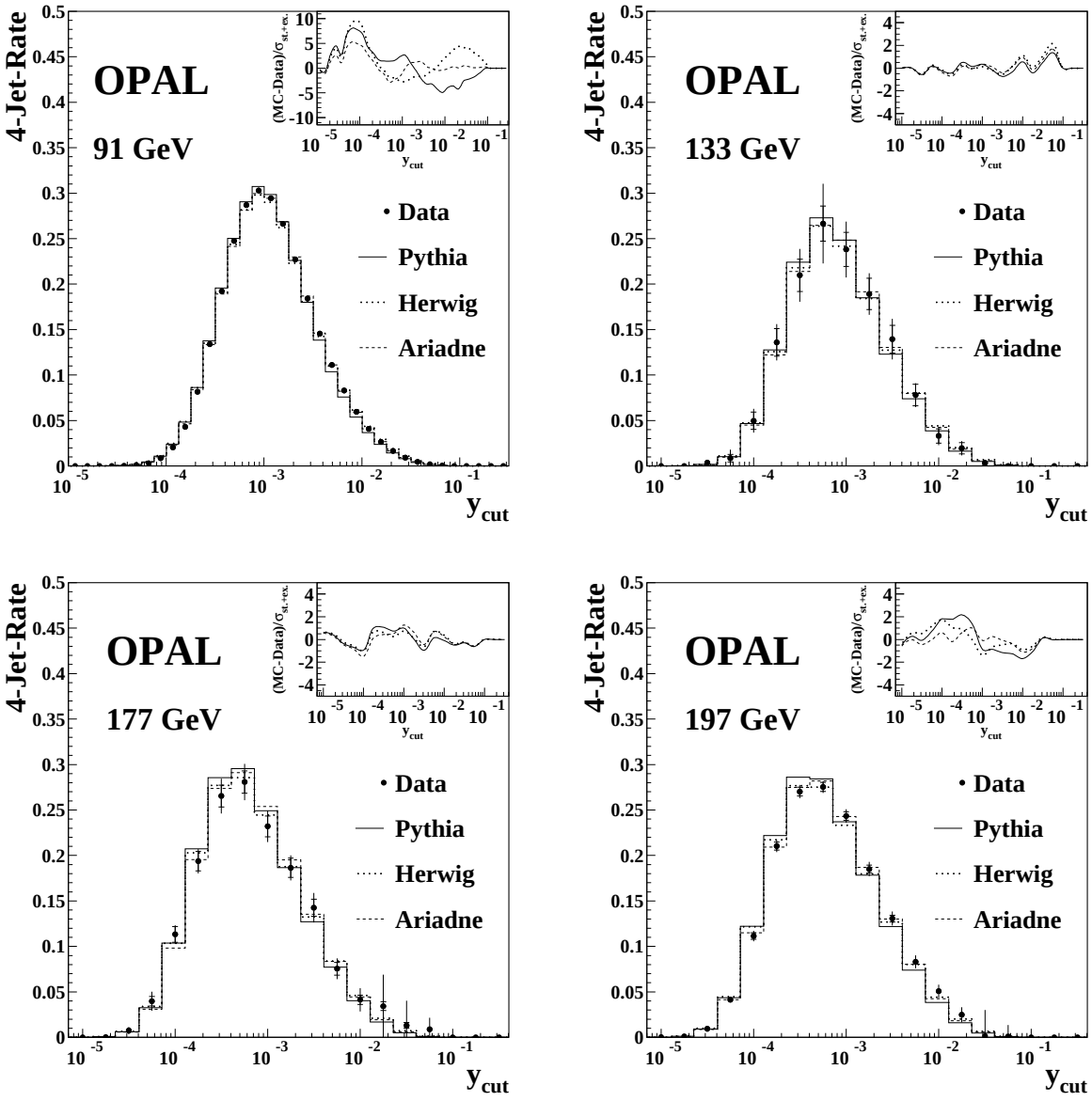

Figure 1: The four-jet rate distribution at hadron level as a function of the $y_{\rm cut}$ resolution parameter obtained with the Durham algorithm. The four-jet rates are shown for the data corrected to the hadron level at four average centre-of-mass energies between 91 and 209 GeV together with predictions based on PYTHIA, HERWIG and ARIADNE Monte Carlo events generated at the averaged energy. The error bars show the statistical (inner error bars) and experimental uncertainties added in quadrature. Error bars not shown are smaller than the point size. The panel in each upper right corner shows the differences between data and Monte Carlo predictions, divided by the sum of the statistical and experimental error. For data points with no data events, the difference is set to zero.

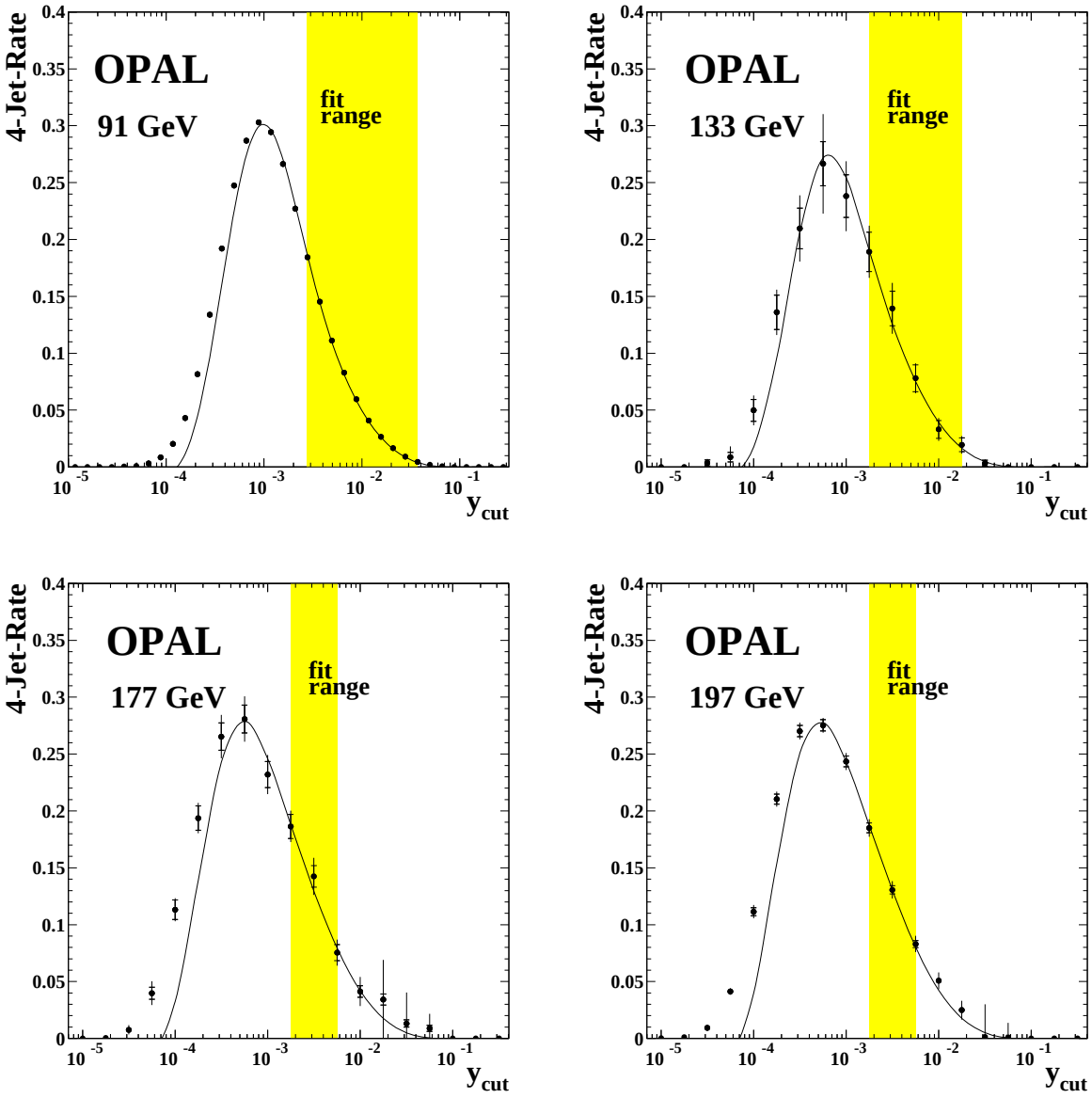

Figure 2: The hadron-level four-jet rate distributions for energies between 91 GeV and 209 GeV. The error bars show the statistical (inner error bars) and experimental uncertainties added in quadrature. When not shown, the errors are smaller than the point size. The curves show the theory prediction after χ^2 minimization within the fit range indicated. The fit range is determined as discussed in Section 5.1.1. The data points are strongly correlated and an enlarged fit range would lead to only a minor gain in statistical precision.

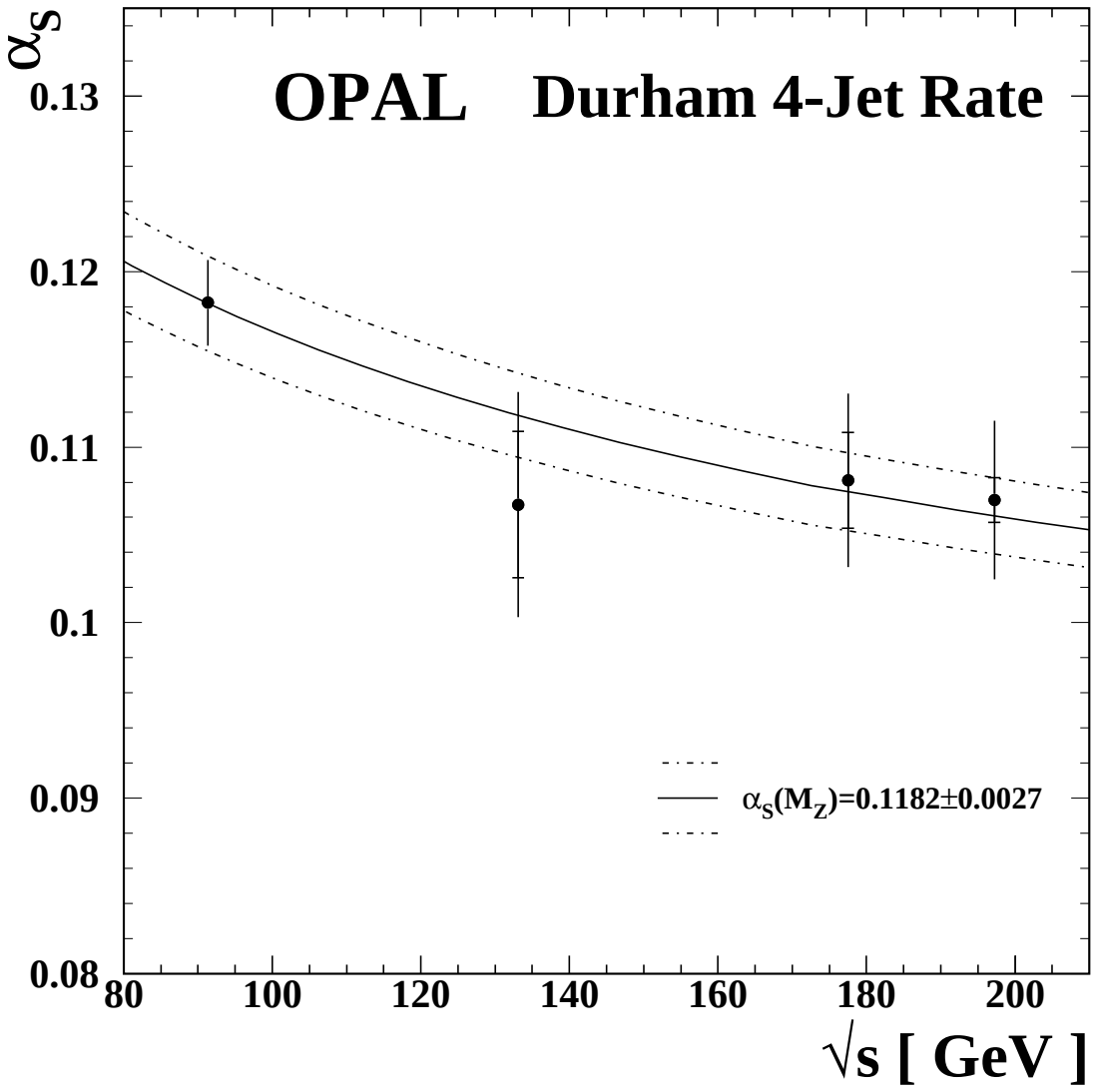

Figure 3: The values for α_S obtained by a fit to the four-jet rate with x_μ set to 1.0 in the four energy intervals. The error bars show the statistical (inner error bars) and the total error. The statistical error at 91 GeV is smaller than the point size. The lines indicate the current world average from [36] with the one standard deviation uncertainty.

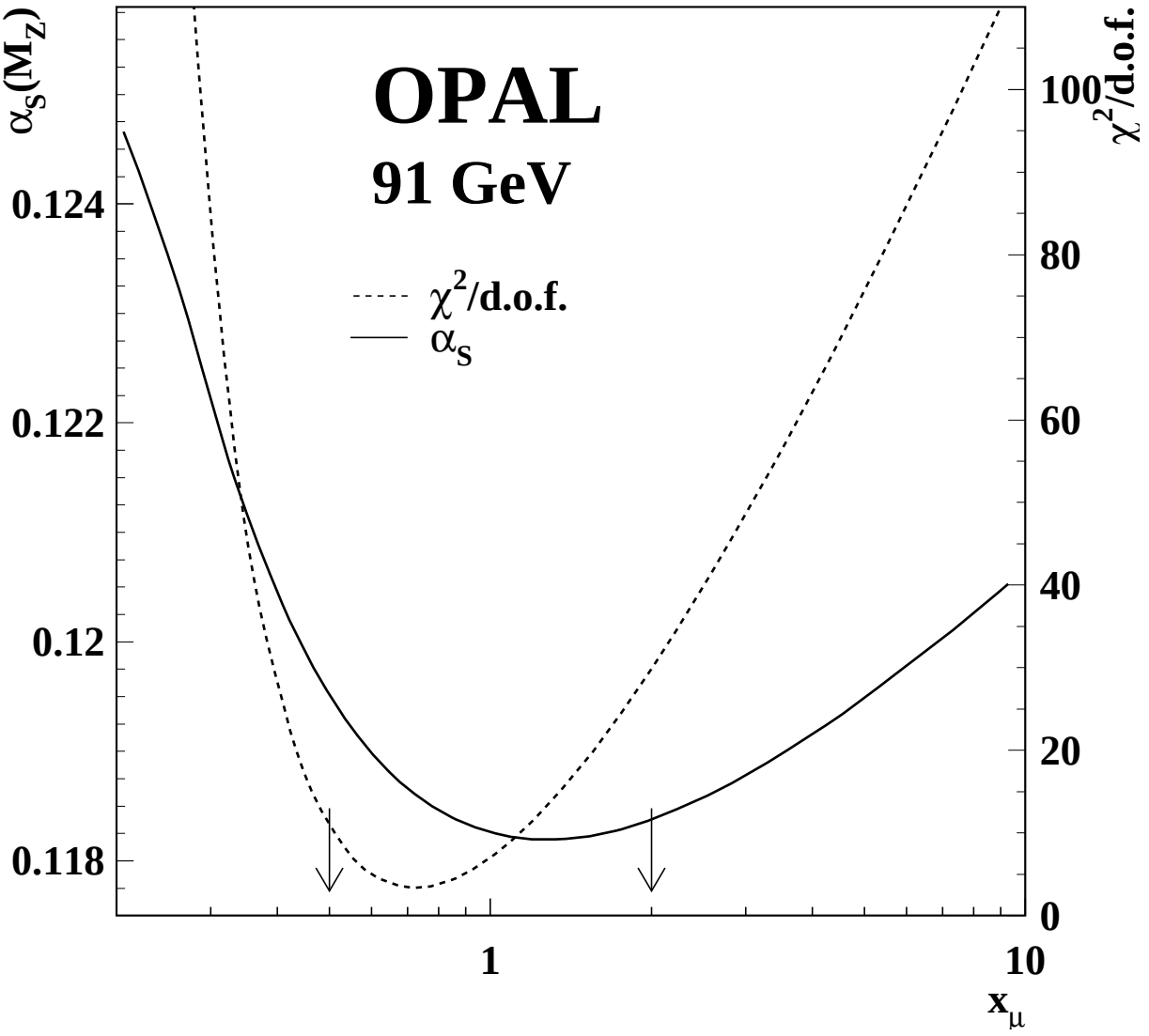

Figure 4: The values of α_S and χ^2/d.o.f. from the fit to the four-jet rate at 91 GeV data as a function of the scale parameter x_μ. The arrows indicate the variation $0.5 < x_\mu < 2.0$ used to determine the theoretical systematic uncertainty.

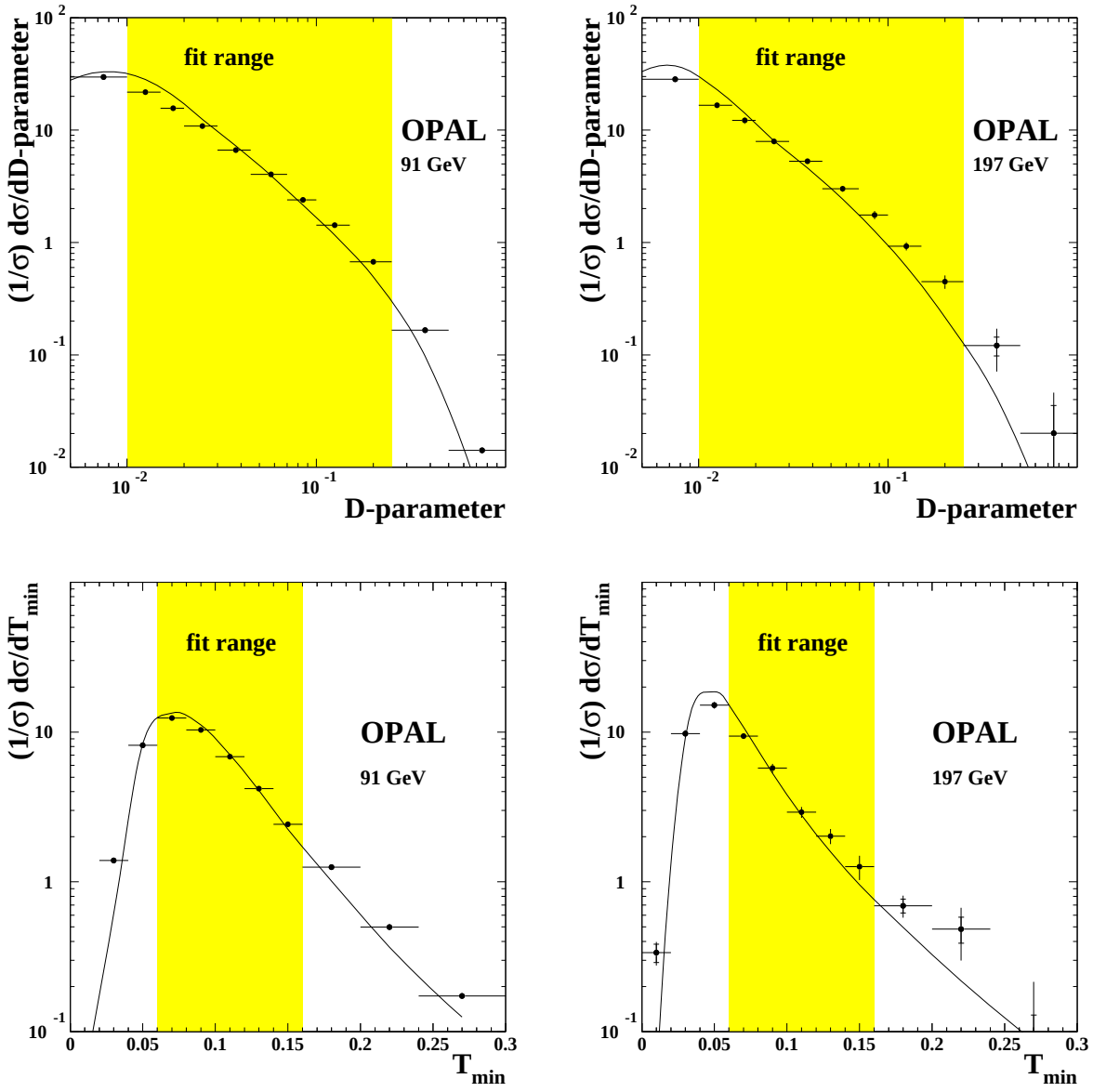

Figure 5: The hadron-level D-parameter and $T_{\rm min}$ distributions for energies of 91 GeV and 197 GeV. The error bars show the statistical (inner error bars) and experimental uncertainties added in quadrature. When not shown, the errors are smaller than the point size. The curves indicate the theory prediction after χ^2-minimization with the renormalization scale set to 1.0. The fit range is determined as discussed in Section 5.2.

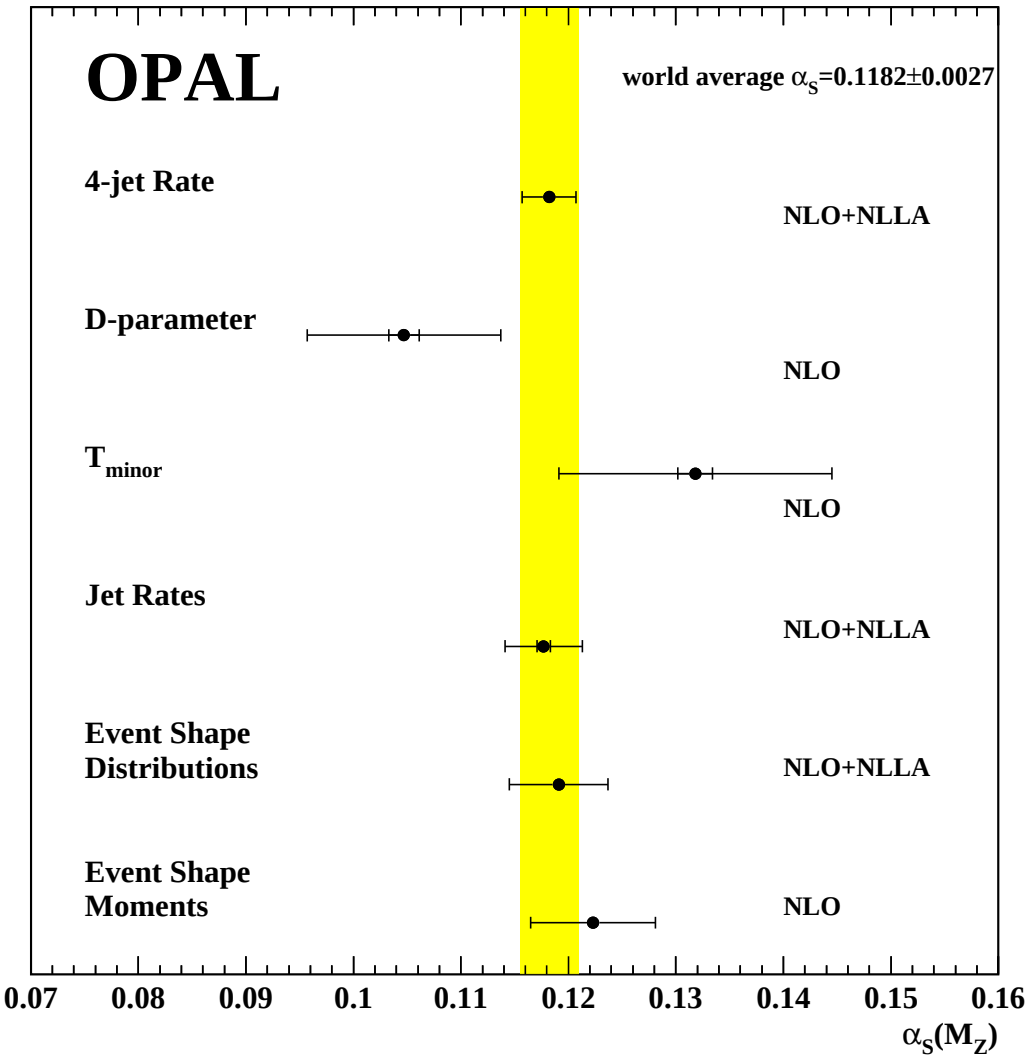

Figure 6: The results of the fit to the four-jet rate, the D-parameter and $T_{\rm min}$. The value of the strong coupling $\alpha_{\rm S}$ obtained from the four-jet rate represents our main result. The analyses of the D-parameter and $T_{\rm min}$ return larger uncertainties as discussed in Section 5.2. Results published by the OPAL collaboration using different predictions and event shapes are shown as well. The value of $\alpha_{\rm S}$ indicated by Jet Rates is obtained by [12]. The results of [13] are indicated as 'Event Shape Distributions' and 'Event Shape Moments'. The type of QCD prediction is indicated in the plot. The $\alpha_{\rm S}$ world average is taken from [36].